LQR-Assisted Whole-Body Control of a Wheeled Bipedal Robot with Kinematic Loops

Victor Klemm, Alessandro Morra, Lionel Gulich, Dominik Mannhart,
David Rohr, Mina Kamel, Yvain de Viragh, and Roland Siegwart

Abstract—We present a hierarchical whole-body controller leveraging the full rigid body dynamics of the wheeled bipedal robot *Ascento*. We derive closed-form expressions for the dynamics of its kinematic loops in a way that readily generalizes to more complex systems. The rolling constraint is incorporated using a compact analytic solution based on rotation matrices. The non-minimum phase balancing dynamics are accounted for by including a linear-quadratic regulator as a motion task. Robustness when driving curves is increased by regulating the lean angle as a function of the zero-moment point. The proposed controller is computationally lightweight and significantly extends the rough-terrain capabilities and robustness of the system, as we demonstrate in several experiments.

Index Terms—Legged Robots, Wheeled Robots, Parallel Robots, Dynamics, Robust/Adaptive Control of Robotic Systems

I. INTRODUCTION

FAST and agile maneuverability is a key component for an efficient deployment of mobile ground robots. In this regard, wheeled-legged systems combine the best of two worlds – they leverage both the speed and efficiency of wheels, and the ability of legs to overcome uneven terrain and obstacles. In recent years, wheeled bipedal robots have started to show the capabilities required for real-world applications [1], while allowing for swift and cost-effective designs, requiring less actuators and being natively able to turn on spot.

The wheeled bipedal robot *Ascento*[1] presented in our previous work [2] is capable of achieving many of the specifications required for typical applications. Being a parallel robot with a four-bar linkage, i.e. a kinematic loop in each of its legs, *Ascento* only requires four actuators, two for driving the wheels and two for moving the legs. This reduces cost, weight, and mechanical complexity, which is desirable for inspection tasks as well as search and rescue applications.

As we have shown, a basic version of these tasks can already be completed with simplified, model-based control strategies [2]. The new linear-quadratic regulator (LQR)-assisted

[1]More information can be found on: https://www.ascento.ethz.ch.

Fig. 1. *Left:* The *Ascento* robot stabilizing while one wheel is placed on an elevated step of height $0.20\,\mathrm{m}$. The four-bar linkage of the left leg is nearly fully extended. *Right:* The robot actively adjusts its legs when driving on uneven terrain, such as the grass slope shown. To see these and many more maneuvers in action we encourage the reader to watch the accompanying video: https://youtu.be/nGu2odkB5ws.

whole-body control (WBC) scheme proposed in this letter extends *Ascento*'s capabilities to outdoor scenarios, rendering the robot more robust to disturbances by active compliance to uneven terrain, as shown in Fig. 1.

A. Related Work

Hierarchical inverse dynamics control (e.g. [3], [4]) and WBC (e.g. [5]–[7]) rapidly gained popularity over the last decade and have been applied to walking robots such as bipeds [8] and quadrupeds [9], [10]. Recent works also showed successful deployment on a wheeled-legged quadruped [11], [12].

However, to the best of the authors' knowledge, application of WBC to stabilization of wheeled bipedal robots and their inherent non-minimumphase dynamics has not been shown before.[2] In our previous work [2], we modeled the robot as a standard two-wheeled inverted pendulum, thereby completely neglecting leg dynamics. We improve this by rigorously treating the kinematic loops in the legs. Typically one approach of the following three is applied for modeling kinematic loops:

1) The system dynamics are derived from an explicit formulation of the kinematics, which is trivial for linkages with a simple geometry [14], but becomes considerably more involved for loops with irregular link lengths [15], such as the one of *Ascento*. Further, this approach is only directly

[2]*Boston Dynamic*'s wheeled bipedal robot *Handle* [13] has demonstrated impressive performance, but, unfortunately, little is known about the underlying control approaches.

applicable to linkages without kinematic inversions in their operating space [16].

2) The system dynamics can be be found by purely numerical techniques, such as the recursive Newton-Euler formulation described in [17]–[19]. However, this approach focuses rather on the simulation than on the derivation of a system's equations of motion (EoM).

3) The loop is opened kinematically and closed by finding appropriate dynamic constraint forces [20], [21].

We build on the third approach because it allows to derive closed-form solutions and can be applied to non-trivial systems.

B. Contribution

Our main contributions can be summarized as follows:

- Derivation of the full rigid body dynamics of a wheeled bipedal robot, with an emphasis on modeling kinematic loops (Section II-C).
- A compact and closed-form rolling constraint formulation using rotation matrices (Section II-D).
- Synthesis of a WBC scheme for control of such robots. Control of the non-minimum phase balancing dynamics is achieved by including an LQR feedback law as a motion task. The robustness against tipping over when driving curves is increased by controlling the leaning angle such that the zero-moment point (ZMP) [22] is shifted towards the center of the line of support (LoS) (Section III).

We demonstrate the performance of our WBC scheme in Section IV and conclude by an outlook on future work in Section V.

II. MODELING

Since the WBC introduced in Section III is a model-based control technique, accurately modeling the system dynamics is key. It should be noted that the approaches presented in this section are generally applicable. For the sake of simplicity, we show them directly for the example of the *Ascento* robot.

A. Coordinates and Conventions

We define the generalized coordinates (Fig. 2), velocities, accelerations, and actuation torques as

$$
\boldsymbol{q} = \begin{bmatrix} {}_I\boldsymbol{r}_{IB} \\ \boldsymbol{R}_{IB} \\ \varphi_1 \\ \vdots \\ \varphi_{n_j} \end{bmatrix}, \ \boldsymbol{u} = \begin{bmatrix} {}_I\boldsymbol{v}_{IB} \\ {}_I\boldsymbol{\omega}_{IB} \\ \dot{\varphi}_1 \\ \vdots \\ \dot{\varphi}_{n_j} \end{bmatrix}, \ \dot{\boldsymbol{u}} = \begin{bmatrix} {}_I\boldsymbol{a}_{IB} \\ {}_I\dot{\boldsymbol{\omega}}_{IB} \\ \ddot{\varphi}_1 \\ \vdots \\ \ddot{\varphi}_{n_j} \end{bmatrix}, \ \boldsymbol{\tau} = \begin{bmatrix} \tau_1 \\ \tau_2 \\ \tau_3 \\ \tau_4 \end{bmatrix},
$$

(1)

respectively, where $\boldsymbol{q} \in \mathbb{R}^3 \times SO(3) \times \mathbb{R}^{n_j}$, $\boldsymbol{u} \in \mathbb{R}^{6+n_j}$, $\dot{\boldsymbol{u}} \in \mathbb{R}^{6+n_j}$ and $\boldsymbol{\tau} \in \mathbb{R}^{n_\tau}$. Thereby, ${}_I\boldsymbol{r}_{IB}$ describes the relative position vector of the frames in the right-hand subscript (i.e. from the inertial frame I to the base frame B), represented in the frame of the left-hand subscript. Similar holds for the linear and angular velocities, and accelerations, i.e. ${}_I\boldsymbol{v}_{IB}$, ${}_I\boldsymbol{\omega}_{IB}$ and ${}_I\boldsymbol{a}_{IB}$, ${}_I\dot{\boldsymbol{\omega}}_{IB}$, respectively. The rotation matrix $\boldsymbol{R}_{IB}$ maps from coordinate representation in frame B to frame I. Further, the
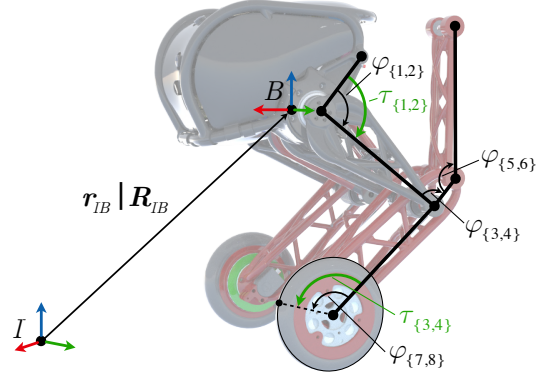

Fig. 2. Generalized coordinates of the system with opened kinematic loops as introduced in (1). The joint angles and actuation torques are marked on the left leg only, and their indices denote the corresponding joint angle on the left- and right-hand side respectively: $\varphi_{\{l,r\}}$, $\tau_{\{l,r\}}$.

scalars φ_i represent the joint angles. In the following, we use superscript brackets (e.g. $\boldsymbol{J}^{(1,3)}$) to indicate specific rows of matrices and $[\cdot]_\times$ for the skew-symmetric cross product matrix of a vector. We use the positional and rotational Jacobian convention

$$
\begin{bmatrix} {}_I\boldsymbol{v}_{IB} \\ {}_I\boldsymbol{\omega}_{IB} \end{bmatrix} = \begin{bmatrix} {}_I\boldsymbol{J}_{IB,\mathcal{P}} \\ {}_I\boldsymbol{J}_{IB,\mathcal{R}} \end{bmatrix} \boldsymbol{u}.
$$

(2)

B. Open-Loop Dynamics

The unconstrained dynamics of the system with opened, kinematic loops can be formulated as

$$
\boldsymbol{M}(\boldsymbol{q})\, \dot{\boldsymbol{u}} + \boldsymbol{b}(\boldsymbol{q},\boldsymbol{u}) + \boldsymbol{g}(\boldsymbol{q}) + \boldsymbol{s}(\boldsymbol{q}) = \boldsymbol{S}^\top \boldsymbol{\tau},
$$

(3)

where $\boldsymbol{M}(\boldsymbol{q}) \in \mathbb{R}^{n_u \times n_u}$ denotes the mass matrix, $\boldsymbol{b}(\boldsymbol{q},\boldsymbol{u}) \in \mathbb{R}^{n_u}$ denotes the vector of Coriolis and centrifugal terms, and $\boldsymbol{g}(\boldsymbol{q}) \in \mathbb{R}^{n_u}$ is the vector of gravity terms.[3] Additionally, $\boldsymbol{s} \in \mathbb{R}^{n_u}$ accounts for the effect of two torsional springs in the knees of the robot. A linear-elastic spring law relating angular deflection and generated torque is assumed. The selection matrix $\boldsymbol{S} \in \mathbb{R}^{n_\tau \times n_u}$ selects on which generalized coordinates the actuation torques $\boldsymbol{\tau}$ are acting. In the following, the direct dependence on the generalized coordinates and velocities is omitted for brevity of notation.

C. Loop Closure

The opened kinematic loop structure is dynamically closed by introducing loop closure forces $\tilde{\boldsymbol{F}}_L$ at the opened hinge points, as shown in Fig. 3. In the following, firstly the derivations are performed exemplary for one loop only, and then applied to both of them.

$\tilde{\boldsymbol{F}}_L$ can be interpreted as bearing forces with their respective reactions acting on the hinge points of the opened loop, P and Q, and are directly added to (3):

$$
\boldsymbol{M}\, \dot{\boldsymbol{u}} + \boldsymbol{b} + \boldsymbol{g} + \boldsymbol{s} + {}_I\boldsymbol{J}_{IP,\mathcal{P}}^\top\, {}_I\tilde{\boldsymbol{F}}_L - {}_I\boldsymbol{J}_{IQ,\mathcal{P}}^\top\, {}_I\tilde{\boldsymbol{F}}_L = \boldsymbol{S}^\top \boldsymbol{\tau}.
$$

(4)

It is to be noted that the loop closure forces should only act in the loop plane Λ, as its normal direction $\boldsymbol{n}_\Lambda$ is already

---

[3]These can, for instance, be calculated using the projected Newton-Euler equations, given the center of mass (CoM) Jacobians and inertial parameters of each body.
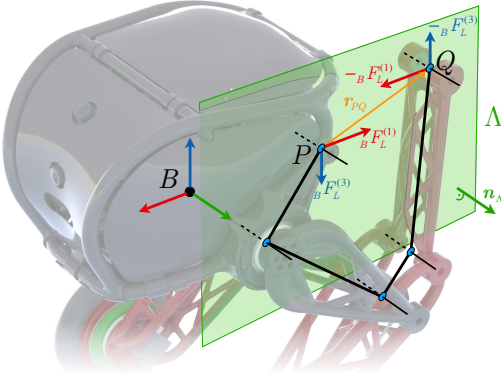
Fig. 3. The opened kinematic loop (of the robot's left side). Indicated are the two hinge points P and Q where the loop has been opened. In order to close the loop, the two equal but opposite loop closure force pairs $\pm_B\boldsymbol{F}_l^{(1)}$ and $\pm_B\boldsymbol{F}_l^{(3)}$ acting in the loop-plane Λ on P and Q must be found.

constrained by the kinematics of the opened loop.[4] Because the robot is a floating-base system, Λ is changing over time. As the loops are fixed and aligned w.r.t. the base frame B, the in-plane components of the loop closure forces can readily be selected: They are directly the x- and z-components of their representation in the base frame,[5] giving

$$\boldsymbol{M}\,\dot{\boldsymbol{u}} + \boldsymbol{b} + \boldsymbol{g} + \boldsymbol{s} + \underbrace{(_B\boldsymbol{J}_{IP,\mathcal{P}}^{(1,3)} - _B\boldsymbol{J}_{IQ,\mathcal{P}}^{(1,3)})^\top}_{:=\tilde{\boldsymbol{J}}_L^\top}{}_B\tilde{\boldsymbol{F}}_L^{(1,3)} = \boldsymbol{S}^\top\boldsymbol{\tau}.$$
(5)

This holds analogous for the left (l) and right (r) kinematic loop, resulting in similar expressions that can be stacked:

$$\boldsymbol{M}\,\dot{\boldsymbol{u}} + \boldsymbol{b} + \boldsymbol{g} + \boldsymbol{s} + \underbrace{\begin{bmatrix}\tilde{\boldsymbol{J}}_{L_l}^\top & \tilde{\boldsymbol{J}}_{L_r}^\top\end{bmatrix}}_{:=\boldsymbol{J}_L^\top}\underbrace{\begin{bmatrix}_B\tilde{\boldsymbol{F}}_{L_l}^{(1,3)} \\ _B\tilde{\boldsymbol{F}}_{L_r}^{(1,3)}\end{bmatrix}}_{:=\boldsymbol{F}_L} = \boldsymbol{S}^\top\,\boldsymbol{\tau}.$$
(6)

To determine the unknown loop closure forces, the position constraint $\boldsymbol{r}_{PQ} = \boldsymbol{0}$ is expressed at acceleration level. Similar to the loop closure forces, it must only be enforced in directions where there are still degrees of freedom (DoFs) to constrain, i.e. only in the loop plane Λ: This is done by the constraint projection $_B\boldsymbol{r}_{PQ}^{(1,3)} = \boldsymbol{0}$. To bring the positional constraint to the acceleration level, two-fold differentiation w.r.t. time is performed, taking care of differentiation in the potentially rotating base frame B:

$$_B\ddot{\boldsymbol{r}}_{PQ} = \frac{d^2}{dt^2}(\boldsymbol{R}_{BI\,I}\boldsymbol{r}_{PQ}) \overset{(1,3)}{=} \boldsymbol{0}, \qquad (7)$$

$$\frac{d}{dt}(\boldsymbol{R}_{BI}\,[_I\boldsymbol{\omega}_{BI}]_\times\,_I\boldsymbol{r}_{PQ} + \boldsymbol{R}_{BI\,I}\boldsymbol{v}_{PQ}) \overset{(1,3)}{=} \boldsymbol{0}. \qquad (8)$$

After the second differentiation step, which is not shown for brevity, the arising terms can be simplified and their formulation can be substituted in terms of the Jacobians.

---

[4]As loop closure forces in direction of $\boldsymbol{n}_\Lambda$ have no effect on the rigid mechanism, they can be of arbitrary size. This leads to rank-deficiency when calculating accelerations, as shown later in Section II-E.

[5]It can be argued that the formulation becomes more general if these components are expressed in the frames attached to one of the opened hinge points P or Q, but the formulation chosen here leads to simpler and more accessible expressions, depending directly on $\boldsymbol{q}$ and $\boldsymbol{u}$.
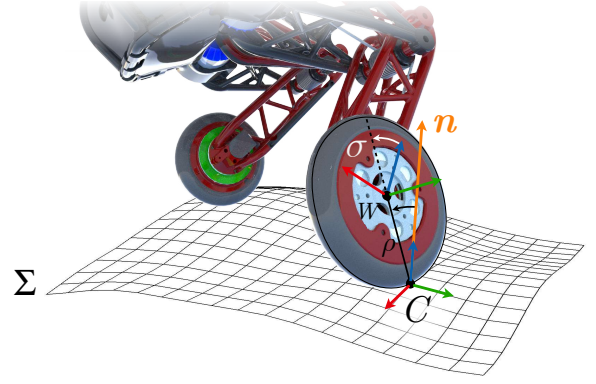

Fig. 4. The ground contact of the (left) wheel with the ground surface Σ. W denotes a wheel-fixed coordinate system and C denotes the frame at the contact point on the wheel's contour, with its position parametrized by the contour parameter σ, and a fixed wheel radius ρ. It is oriented with its z-axis along the current ground normal direction $\boldsymbol{n}$ and its x-axis along the heading direction of the wheel.

This allows to factor out $\boldsymbol{u}$ and $\dot{\boldsymbol{u}}$, yielding a constraint on acceleration level[6]

$$\tilde{\boldsymbol{X}}\boldsymbol{u} + \tilde{\boldsymbol{Y}}\dot{\boldsymbol{u}} \overset{(1,3)}{=} \boldsymbol{0}, \quad \text{where} \qquad (9)$$

$$\tilde{\boldsymbol{X}} = \boldsymbol{R}_{BI}\big(-[_I\boldsymbol{\omega}_{IB}]_\times\,[_I\boldsymbol{r}_{PQ}]_\times\,_I\boldsymbol{J}_{IB,\mathcal{R}} + [_I\boldsymbol{r}_{PQ}]_\times\,_I\dot{\boldsymbol{J}}_{IB,\mathcal{R}}$$
$$- 2\,[_I\boldsymbol{\omega}_{IB}]_\times\,_I\boldsymbol{J}_{PQ,\mathcal{P}} + {}_I\dot{\boldsymbol{J}}_{PQ,\mathcal{P}}\big), \qquad (10)$$

$$\tilde{\boldsymbol{Y}} = \boldsymbol{R}_{BI}([_I\boldsymbol{r}_{PQ}]_\times\,_I\boldsymbol{J}_{IB,\mathcal{R}} + {}_I\boldsymbol{J}_{PQ,\mathcal{P}}). \qquad (11)$$

Constraint (9) is applied to both kinematic loops and stacked:

$$\underbrace{\begin{bmatrix}\tilde{\boldsymbol{X}}_l^{(1,3)} \\ \tilde{\boldsymbol{X}}_r^{(1,3)}\end{bmatrix}}_{:=\boldsymbol{X}}\boldsymbol{u} + \underbrace{\begin{bmatrix}\tilde{\boldsymbol{Y}}_l^{(1,3)} \\ \tilde{\boldsymbol{Y}}_r^{(1,3)}\end{bmatrix}}_{:=\boldsymbol{Y}}\dot{\boldsymbol{u}} = \boldsymbol{0}, \qquad (12)$$

giving the loop closure constraint in its final formulation. It will then be used in conjunction with the ground contact constraint introduced in the next section to simultaneously determine all missing constraint forces as shown in Section II-E.

D. Ground Contacts

To constrain the wheels' motion on the ground surface, firstly a general formulation of the rolling constraint based on rotation matrices[7] is introduced, and then the corresponding constraint forces are derived. Again the equations are shown exemplary for one wheel and then applied to both of them.

In contrast to a point contact foot, where the area of potential contact locations is restricted to a single point, in the case of a wheel it spans the entire circumference (modeled as flat disk). Inspired by the notion of contour-kinematics introduced in [23], we parametrize the position of the contact point C on the contour of the wheel by a contour parameter σ, as shown in Fig. 4. The velocity of C can be expressed by

---

[6]It should be observed that $_B\boldsymbol{r}_{PQ}$ is explicitly contained in these equations. In fact, the derivation yields the same result when starting with $_B\boldsymbol{r}_{PQ} = \text{const}$. In other words, the presented constraint formulation correctly captures the dynamics for arbitrary values of $_B\boldsymbol{r}_{PQ}$. This could explain why we did not experience problems due to divergence caused by numerical errors opening the kinematic loop, which, typically, is counteracted by using Baumgarte's stabilization technique [20].

[7]In contrast to e.g. [11], where a set of local Euler angles is used.

$$_I\boldsymbol{v}_{IC}(\sigma) = {}_I\boldsymbol{v}_{IW} + \underbrace{[{}_I\boldsymbol{\omega}_{IW}]_\times \, _I\boldsymbol{r}_{WC}(\sigma)}_{_I\boldsymbol{v}_{WC}(\sigma)}, \qquad (13)$$

$$\text{where} \quad _I\boldsymbol{r}_{WC}(\sigma) = \boldsymbol{R}_{IW} \underbrace{\begin{bmatrix} \rho\sin(\sigma) & 0 & \rho\cos(\sigma) \end{bmatrix}^\top}_{_W\boldsymbol{r}_{WC}(\sigma)}, \quad (14)$$

where ρ denotes the wheel radius, and where $_I\boldsymbol{v}_{IW}$, $_I\boldsymbol{\omega}_{IW}$ and $\boldsymbol{R}_{IW}$ can be obtained from forward differential kinematics. The contour parameter σ can directly be calculated from the current normal vector of the ground surface:

$$\sigma(_I\boldsymbol{n}) = \arctan2(\boldsymbol{R}_{WI}^{(1)} \, _I\boldsymbol{n}, \ \boldsymbol{R}_{WI}^{(3)} \, _I\boldsymbol{n}). \qquad (15)$$

To impose a constraint on the velocity of C that can be used to find the contact forces, the constraint must be formulated on the acceleration level. We therefore differentiate (13) w.r.t. time, which gives

$$_I\boldsymbol{a}_{IC}(\sigma, \ \dot\sigma) = {}_I\boldsymbol{a}_{IW} + {}_I\boldsymbol{a}_{WC}(\sigma, \ \dot\sigma), \qquad (16)$$

where from $_I\boldsymbol{v}_{WC}$, as given in (13), we obtain[8]

$$_I\boldsymbol{a}_{WC}(\sigma, \ \dot\sigma) = [{}_I\dot{\boldsymbol{\omega}}_{IW}]_\times \, _I\boldsymbol{r}_{WC}(\sigma) + [{}_I\boldsymbol{\omega}_{IW}]_\times^2 \, _I\boldsymbol{r}_{WC}(\sigma)$$
$$+ [{}_I\boldsymbol{\omega}_{IW}]_\times \, \boldsymbol{R}_{IW} \underbrace{\frac{d}{d\sigma} \, _W\boldsymbol{r}_{WC}(\sigma)}_{:=_W\boldsymbol{t}} \dot\sigma. \quad (17)$$

A closed form expression for $\dot\sigma$ can be found by differentiating (15), which is made possible by the continuous differentiability of $\arctan2$. Application of the chain rule gives

$$\dot\sigma(_I\boldsymbol{n}, \ _I\dot{\boldsymbol{n}}) = \frac{d\sigma}{d(\boldsymbol{R}_{WI}\,_I\boldsymbol{n})}([{}_W\boldsymbol{\omega}_{WI}]_\times \, \boldsymbol{R}_{WI}\,_I\boldsymbol{n} + \boldsymbol{R}_{WI}\,_I\dot{\boldsymbol{n}}). \tag{18}$$

If $_I\dot{\boldsymbol{n}}$ is assumed to be $\boldsymbol{0}$,[9] $\boldsymbol{u}$ and $\dot{\boldsymbol{u}}$ can be factored out of (16), resulting in the Jacobian formulation

$$_I\boldsymbol{a}_{IC}(\sigma, \ \dot\sigma) = {}_I\dot{\boldsymbol{J}}_{IC,\mathcal{P}}(\sigma)\,\boldsymbol{u} + {}_I\boldsymbol{J}_{IC,\mathcal{P}}(\sigma)\,\dot{\boldsymbol{u}}. \qquad (19)$$

For perfect rolling, a zero acceleration constraint must be enforced in the x- and z-directions of the contact frame, i.e.

$$_C\dot{\boldsymbol{J}}_{IC,\mathcal{P}}(\sigma)\,\boldsymbol{u} + {}_C\boldsymbol{J}_{IC,\mathcal{P}}(\sigma)\,\dot{\boldsymbol{u}} \overset{(1,3)}{=} \boldsymbol{0}. \qquad (20)$$

All of the above derivations can be performed analogously for the left- and the right-hand side, which allows stacking of the obtained quantities:

$$\underbrace{\begin{bmatrix} _{C_l}\boldsymbol{J}_{IC_l,\mathcal{P}}^{(1,3)} \\ _{C_r}\boldsymbol{J}_{IC_r,\mathcal{P}}^{(1,3)} \end{bmatrix}}_{:=\boldsymbol{J}_A} \boldsymbol{u} + \underbrace{\begin{bmatrix} _{C_l}\dot{\boldsymbol{J}}_{IC_l,\mathcal{P}}^{(1,3)} \\ _{C_r}\dot{\boldsymbol{J}}_{IC_r,\mathcal{P}}^{(1,3)} \end{bmatrix}}_{:=\dot{\boldsymbol{J}}_A} \dot{\boldsymbol{u}} = \boldsymbol{0}. \qquad (21)$$

As the robot is capable of leaning to its sides, the distance of the two contact points of the wheels does not remain constant.

[8]We note that $_W\boldsymbol{t}$ points along the current tangential direction of the wheel contour. The expression containing $_W\boldsymbol{t}$ can be interpreted as a compensation term for the centripetal acceleration that a wheel-fixed point experiences as it moves with the wheel.

[9]If this is not the case, $_I\dot{\boldsymbol{n}}$ can be appended to the generalized velocity vector $\boldsymbol{u}$ to achieve the linear Jacobian relationship of (19). We note that the current ground surface estimation can then be formulated as a constrained state estimation problem. However, this is beyond the scope of this letter.

Therefore, slipping occurs in the y-directions of the contact frames, leading to friction forces acting along

$$\boldsymbol{J}_F := \begin{bmatrix} _{C_l}\boldsymbol{J}_{IC_l,\mathcal{P}}^{(2)} \\ _{C_r}\boldsymbol{J}_{IC_r,\mathcal{P}}^{(2)} \end{bmatrix}. \qquad (22)$$

Now, rolling constraint forces $\boldsymbol{F}_C \in \mathbb{R}^4$ and friction terms are added to (6):

$$\boldsymbol{M}\dot{\boldsymbol{u}}+\boldsymbol{b}+\boldsymbol{g}+\boldsymbol{s}+\boldsymbol{J}_L^\top\,\boldsymbol{F}_L+\boldsymbol{J}_A^\top\,\boldsymbol{F}_C+\boldsymbol{J}_F^\top\,\boldsymbol{C}_F\,\boldsymbol{F}_C = \boldsymbol{S}^\top\boldsymbol{\tau}, \ (23)$$

where $\boldsymbol{C}_F$ represents a velocity dependent friction curve which we model by the differentiable $\tanh$-function, with μ_s being the sliding friction coefficient between tires and ground:

$$\boldsymbol{C}_F = -\mu_s \begin{bmatrix} 0 & \tanh(\boldsymbol{J}_F^{(1)}\,\boldsymbol{u}) & 0 & 0 \\ 0 & 0 & 0 & \tanh(\boldsymbol{J}_F^{(2)}\,\boldsymbol{u}) \end{bmatrix}. \quad (24)$$

E. Solving for the Unknown Constraint Forces

To state the complete EoM, all that is left is to determine the unknown constraint forces in (23) with the aid of the constraints (12) and (21). For this purpose, we first stack the unknown forces and the corresponding constraints:

$$\boldsymbol{M}\dot{\boldsymbol{u}}+\boldsymbol{b}+\boldsymbol{g}+\boldsymbol{s}+\underbrace{\begin{bmatrix} \boldsymbol{J}_L \\ \boldsymbol{J}_A+\boldsymbol{C}_F^\top\boldsymbol{J}_F \end{bmatrix}^\top}_{:=\boldsymbol{J}} \underbrace{\begin{bmatrix} \boldsymbol{F}_L \\ \boldsymbol{F}_C \end{bmatrix}}_{:=\boldsymbol{F}} = \boldsymbol{S}^\top\boldsymbol{\tau}, \quad (25)$$

$$\underbrace{\begin{bmatrix} \boldsymbol{X}^\top & \boldsymbol{J}_A^\top \end{bmatrix}^\top}_{:=\boldsymbol{V}} \boldsymbol{u} + \underbrace{\begin{bmatrix} \boldsymbol{Y}^\top & \boldsymbol{J}_A^\top \end{bmatrix}^\top}_{:=\boldsymbol{W}} \dot{\boldsymbol{u}} = \boldsymbol{0}. \qquad (26)$$

Next, (25) can be solved for $\dot{\boldsymbol{u}}$, which can be inserted in (26) and then solved for the constraint forces, resulting in

$$\boldsymbol{F} = (\boldsymbol{W}\boldsymbol{M}^{-1}\boldsymbol{J}^\top)^{-1}(\boldsymbol{V}\boldsymbol{u} + \boldsymbol{W}\boldsymbol{M}^{-1}(\boldsymbol{S}^\top\boldsymbol{\tau} - \boldsymbol{b} - \boldsymbol{g} - \boldsymbol{s})). \tag{27}$$

By substituting, the final EoM of the system are obtained.

III. CONTROL

A. Whole-Body Control

The WBC-problem in its basic form can be written as a hierarchical quadratic optimization, see for instance [6],

$$\boldsymbol{x}_i = \underset{\boldsymbol{x}}{\arg\min} \ \|\boldsymbol{A}_i\,\boldsymbol{x} - \boldsymbol{b}_i\|_2^2 \qquad (28)$$

$$\text{s.t.} \begin{bmatrix} \boldsymbol{A}_1 \\ \vdots \\ \boldsymbol{A}_{i-1} \end{bmatrix} \boldsymbol{x} = \begin{bmatrix} \boldsymbol{A}_1\,\boldsymbol{x}_1 \\ \vdots \\ \boldsymbol{A}_{i-1}\,\boldsymbol{x}_{i-1} \end{bmatrix}, \begin{bmatrix} \boldsymbol{C}_1 \\ \vdots \\ \boldsymbol{C}_{n_{ineq}} \end{bmatrix} \boldsymbol{x} \le \begin{bmatrix} \boldsymbol{d}_1 \\ \vdots \\ \boldsymbol{d}_{n_{ineq}} \end{bmatrix}, \tag{29}$$

where in each iteration i a task is added. In the context of this work, a task is defined as a linear equality $\boldsymbol{A}_i\,\boldsymbol{x} = \boldsymbol{b}_i$ which is to be satisfied as accurately as possible with regard to the 2-norm. By expanding the objective, each iteration of (28) subject to (29) is formulated as a quadratic program (QP)

$$\underset{\boldsymbol{x}}{\arg\min} \ \frac{1}{2}\boldsymbol{x}^\top\boldsymbol{H}\boldsymbol{x} + \boldsymbol{f}^\top\boldsymbol{x} \quad \text{s.t.} \ \boldsymbol{A}\boldsymbol{x} = \boldsymbol{b}, \ \boldsymbol{C}\boldsymbol{x} \le \boldsymbol{d}, \quad (30)$$

where we define the optimization variables as

$$\boldsymbol{x} = \begin{bmatrix} \dot{\boldsymbol{u}}^\top & \boldsymbol{F}_L^\top & \boldsymbol{F}_C^\top & \boldsymbol{\tau}^\top \end{bmatrix}^\top. \qquad (31)$$

After completing the last iteration, the actuation torques $\boldsymbol{\tau}$ are directly applied to the system.

B. Motion, Force and Torque Tasks

In the following, we list the motion, force, and torque tasks in hierarchical order, from highest to lowest priority.

1) Dynamics Model: In order for the motion to remain physical, the optimization variables in $\boldsymbol{x}$ must satisfy the constrained EoM (25) and (26):

$$\boldsymbol{A}_1 = \begin{bmatrix} \boldsymbol{M} & \boldsymbol{J}_L^\top & \boldsymbol{J}_A^\top + \boldsymbol{J}_F^\top \boldsymbol{C}_F & -\boldsymbol{S}^\top \\ \boldsymbol{W} & \boldsymbol{0} & \boldsymbol{0} & \boldsymbol{0} \end{bmatrix}, \boldsymbol{b}_1 = \begin{bmatrix} -\boldsymbol{b} - \boldsymbol{g} - \boldsymbol{s} \\ -\boldsymbol{V}\boldsymbol{u} \end{bmatrix} \tag{32}$$

2) Base Height: This task controls the height of the base w.r.t. a local control frame N – similar to the one in [9] – which has x-axis aligned with the robot's heading direction, y-axis pointing along the LoS, and origin at the midpoint G thereof. The task on acceleration level is given by

$$\boldsymbol{A}_2 = \begin{bmatrix} {}_N\boldsymbol{J}_{NB,\mathcal{P}}^{(3)} & \boldsymbol{0} & \boldsymbol{0} & \boldsymbol{0} \end{bmatrix}, \boldsymbol{b}_2 = {}^{des}_N\ddot{\boldsymbol{r}}_{NB}^{(3)} - {}_N\dot{\boldsymbol{J}}_{NB,\mathcal{P}}^{(3)}\boldsymbol{u}, \tag{33}$$

where the desired operational space acceleration ${}^{des}_N\ddot{\boldsymbol{r}}_{NB}^{(3)}$ is controlled along a reference trajectory by a proportional-derivative (PD)-law

$$\begin{aligned} {}^{des}_N\ddot{\boldsymbol{r}}_{NB}^{(3)} = {}&k_p\big({}^{ref}_N\boldsymbol{r}_{NB}^{(3)} - {}_N\boldsymbol{r}_{NB}^{(3)}\big) \\ &+ k_d\big({}^{ref}_N\dot{\boldsymbol{r}}_{NB}^{(3)} - {}_N\dot{\boldsymbol{r}}_{NB}^{(3)}\big) + {}^{ref}_N\ddot{\boldsymbol{r}}_{NB}^{(3)}, \end{aligned} \tag{34}$$

where k_p and k_d denote the respective gains. We modify ${}^{ref}_N\boldsymbol{r}_{NB}^{(3)}$ to take the current roll and pitch angles into account, in order to let the system behave like an inverted pendulum with fixed length.

3) Base Roll Angle: This task controls the roll angle ψ of the base. This allows the robot to maintain a prespecified roll orientation, even if the extensions of the legs change, for instance due to unmodeled uneven terrain, as shown in IV-B2. The task on acceleration level is given by

$$\boldsymbol{A}_3 = \begin{bmatrix} {}_N\boldsymbol{J}_{NB,\mathcal{R}}^{(1)} & \boldsymbol{0} & \boldsymbol{0} & \boldsymbol{0} \end{bmatrix}, \boldsymbol{b}_3 = {}^{des}\ddot{\psi} - {}_N\dot{\boldsymbol{J}}_{NB,\mathcal{R}}^{(1)}\boldsymbol{u}, \tag{35}$$

where the desired roll acceleration ${}^{des}\ddot{\psi}$ is again controlled along a reference trajectory by a PD-law analogous to (34).

For a bipedal system, driving tight curves is possible, but can lead to loss of robustness against tipping over. To counteract this effect we compute the roll angle reference such that the ZMP comes to lie at G,[10] as shown in Fig. 5.

4) LQR-Assisted Balancing: The direct application of WBC to systems with non-minimum phase dynamics, as in the case of a wheeled balancing robot, can be problematic. This is illustrated by the following example: For the base to accelerate forwards from the upright position, the wheels first need to accelerate backwards to achieve sufficient pitch angle and should only then accelerate forwards, to avoid falling over. In its standard form, WBC fails to reproduce this behavior since it computes accelerations in the direction of the desired

[10] The centering of the ZMP could also be achieved by adding a task requiring the normal forces of both wheels to be equal, but the chosen approach enables tuning of the leaning aggressiveness. Further, it would also be possible to tune the equality constraint on the normal forces by adding it to the objective of the WBC as a soft constraint.
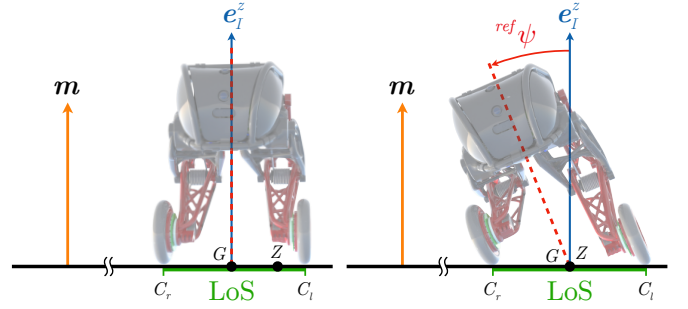

Fig. 5. Curve driving of the robot around the axis of rotation $\boldsymbol{m}$. *Left:* The system drives without adjusting its roll-angle reference ${}^{ref}\psi$. The larger the linear and angular velocities are, the more the ZMP moves outwards towards the endpoint of the current LoS, causing the robot to gradually lose robustness against tipping over. *Right:* The roll-angle reference ${}^{ref}\psi$ is adjusted such that the ZMP coincides with the center G of the LoS, thereby increasing the robustness of the robot against falling sideways.

motion only. We propose to overcome this issue by including an LQR feedback law as a motion task, shown in the following.

Firstly, a simplified model (seen in Fig. 6) is created which captures the essential dynamics of a two-wheeled inverted pendulum system, i.e. the coupling of the tilting and driving motions. This results in a lumped pendulum body Π with pitch angle θ and average wheel hub velocity v. We define ${}^{des}\ddot{\theta}$ as the input to the simplified system, as this is the quantity the WBC will be tracking. The simplified system is then linearized at the current operating point,[11] resulting in a state-space system of the form

$$\begin{bmatrix} \dot{\theta} \\ \ddot{\theta} \\ \dot{v} \end{bmatrix} = \begin{bmatrix} 0 & 1 & 0 \\ 0 & 0 & 0 \\ a_{3,1} & a_{3,2} & 0 \end{bmatrix} \begin{bmatrix} \theta \\ \dot{\theta} \\ v \end{bmatrix} + \begin{bmatrix} 0 \\ 1 \\ b_{3,1} \end{bmatrix} {}^{des}\ddot{\theta}, \tag{36}$$

where $a_{3,1}$, $a_{3,2}$, and $b_{3,1}$ are functions of the lumped inertias, lumped masses and the lumped pendulum length, evaluated at each time step T_s of the controller. (36) is then discretized, assuming zero-order hold (ZOH) over T_s. Finally, the discrete time algebraic Riccati equation (DARE) is solved for the discretized system, yielding the infinite-horizon controller gain matrix $\boldsymbol{K} = \begin{bmatrix} k_\theta & k_{\dot{\theta}} & k_v \end{bmatrix}$. The corresponding feedback law

$$ {}^{des}\ddot{\theta} = k_\theta\big({}^{ref}\theta - \theta\big) + k_{\dot{\theta}}\big({}^{ref}\dot{\theta} - \dot{\theta}\big) + k_v\big({}^{ref}v - v\big) \tag{37}$$

can be used to track a reference trajectory, e.g. a positive ground velocity. The controller will then respond with the desired motion, i.e. first driving backwards a little and then accelerating forwards.

To include (37) in a WBC-task, we track ${}^{des}\ddot{\theta}$ by deriving an approximated lumped rotational Jacobian ${}_N\boldsymbol{J}_{N\Pi,\mathcal{R}}$ for the lumped pendulum body Π. We start by using the notion of average angular momentum introduced in [24] to lump all bodies (n_{bod}) except for the two wheels together, approximating it as

$${}_I\boldsymbol{I}_\Pi {}_I\boldsymbol{\omega}_{I\Pi} = \sum_{K=1}^{n_{bod}-2} {}_I\boldsymbol{I}_K {}_I\boldsymbol{\omega}_{I\Pi} = \sum_{K=1}^{n_{bod}-2} {}_I\boldsymbol{I}_K {}_I\boldsymbol{\omega}_{IK}, \tag{38}$$

[11] The required accelerations $\dot{\boldsymbol{u}}$ are calculated using (25), (27) from the current system state $\boldsymbol{q}$, $\boldsymbol{u}$.
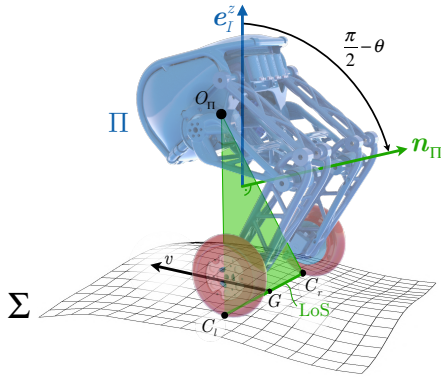
Fig. 6. Relevant quantities of the simplified system used for synthesis of the LQR control law. The base and the leg structures (i.e. all rigid bodies except the wheels) are lumped into a substitute pendulum body Π. The pitch angle θ of Π can be found by spanning a plane with normal $\boldsymbol{n}_\Pi$ between the CoM of Π (O_Π) and the two contact points of the wheels. Thereof, θ can be extracted such that $\theta = 0$ if $\boldsymbol{n}_\Pi$ and $\boldsymbol{e}_I^z$ (i.e. the z-direction of the I frame) are orthogonal, or in other words, if O_Π lies above the LoS. This notion allows stability also when balancing with wheels on different heights (shown in Fig. 9), or when leaning into curves (as in Fig. 10). Further, v is defined as the average wheel hub velocity in the current heading direction and can be interpreted as the ground velocity of the system.

where $_I\boldsymbol{I}_K$ denotes the inertia tensor at the CoM-frame of body K represented in frame I. By rewriting (38) in Jacobian form, the lumped rotational Jacobian can be defined as

$$_I\boldsymbol{J}_{I\Pi,\mathcal{R}} = (_I\boldsymbol{I}_\Pi)^{-1} \sum_{K=1}^{n_{bod}-2} {_I\boldsymbol{I}_K} \, {_I\boldsymbol{J}_{IK,\mathcal{R}}}. \tag{39}$$

Similarly, $_I\dot{\boldsymbol{J}}_{I\Pi,\mathcal{R}}$ is found, which enables the formulation of a motion task for $\ddot{\theta}$ in the control frame N as

$$\boldsymbol{A}_4 = \begin{bmatrix} _N\boldsymbol{J}_{N\Pi,\mathcal{R}}^{(2)} & \boldsymbol{0} & \boldsymbol{0} & \boldsymbol{0} \end{bmatrix}, \; \boldsymbol{b}_4 = {^{des}\ddot{\theta}} - {_N\dot{\boldsymbol{J}}_{N\Pi,\mathcal{R}}^{(2)}}\boldsymbol{u}. \tag{40}$$

5) Base Yaw Angle: This task controls the yaw angle ϕ of the base, and therefore the robot's heading direction. The task on acceleration level is given by

$$\boldsymbol{A}_5 = \begin{bmatrix} _N\boldsymbol{J}_{NB,\mathcal{R}}^{(3)} & \boldsymbol{0} & \boldsymbol{0} & \boldsymbol{0} \end{bmatrix}, \; \boldsymbol{b}_5 = {^{des}\ddot{\phi}} - {_N\dot{\boldsymbol{J}}_{NB,\mathcal{R}}^{(3)}}\boldsymbol{u}, \tag{41}$$

whereby the desired yaw acceleration $^{des}\ddot{\phi}$ is controlled by a feedback law analogous to (34).

6) Actuation Torque Minimization: A unique solution is enforced by minimizing all actuation torques (and thereby also the robot's power consumption):

$$\boldsymbol{A}_6 = \begin{bmatrix} \boldsymbol{0} & \boldsymbol{0} & \boldsymbol{0} & \mathbb{I}_{n_\tau \times n_\tau} \end{bmatrix}, \; \boldsymbol{b}_6 = \boldsymbol{0}, \tag{42}$$

where $\mathbb{I}_{n_\tau \times n_\tau}$ denotes the $n_\tau \times n_\tau$ identity matrix.

C. Inequality Constraints

In the following, we list the inequality constraints contributing to (29). Since they are enforced at every hierarchy level, their ordering does not matter.

1) Actuator Saturation: Joint torques are constrained by the bi-directional actuator saturation bounds $-^{sat}\boldsymbol{\tau} \leq \boldsymbol{\tau} \leq {^{sat}\boldsymbol{\tau}}$.

2) Unilateral Contact Forces: To prevent the robot from "pulling" on the ground, we add the following two inequality constraints $\boldsymbol{F}_C^{(2)} \leq 0$ and $\boldsymbol{F}_C^{(4)} \leq 0$.
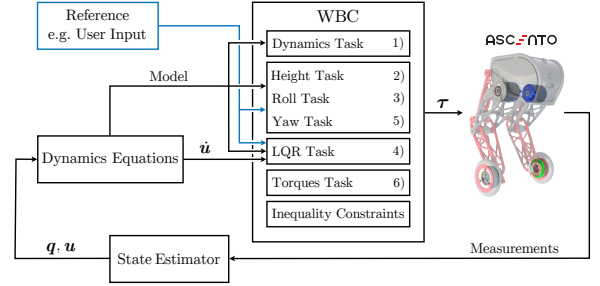

Fig. 7. Block diagram of the control pipeline running on the robot.

3) Static Friction: To prevent slipping in rolling direction, we constrain the corresponding friction forces to stay within the static friction bounds $\pm\boldsymbol{F}_C^{(1)} \leq -\mu_h\boldsymbol{F}_C^{(2)}$ and $\pm\boldsymbol{F}_C^{(3)} \leq -\mu_h\boldsymbol{F}_C^{(4)}$, where μ_h is the coefficient of static friction.

IV. RESULTS AND DISCUSSION

The modeling and control approaches presented in this work were first validated in a custom *MATLAB* simulation and in *Gazebo* [25] with *ODE* [26] as physics back-end, and then tested on hardware, that is, the *Ascento* robot. In the following, we outline the implementation details of the control pipeline – including the state estimation – and show three selected experiments. These, and additional ones, are also presented in the accompanying video.

A. Setup

1) State Estimation: Through the robot's sensors, i.e. an Inertial Measurement Unit (IMU) (with an integrated filter) mounted to the base and rotational encoders at each of the four motors, we can kinematically reconstruct the state of the robot up to its absolute position $\boldsymbol{r}_{IB}$ and velocity $\boldsymbol{v}_{IB}$.[12] We therefore use the contact point of the left wheel as a reference, inspired by [27], getting its absolute position and velocity through a wheel odometry estimate, assuming ground contact for all times. To reflect this choice also in the model, we adjust the contact situation at the wheels by removing sliding friction and adding a (slightly unphysical) hard contact constraint in the y-direction of the left wheel's contact frame. Approaches to circumvent this problem in the scope of future work are discussed in Section V. Further, the ground is considered locally flat for modeling.

2) Implementation: The dynamics model[13] and the WBC[14] were implemented in ROS/C++ using *Eigen* as linear algebra library [28]. For the dynamics model – in particular the computation of the Jacobians – we used a custom formulation

---

[12]Estimation of the missing quantities by integration leads to poor results due to the high measurement noise of the IMU.

[13]The geometrical and inertial parameters were obtained from the computer-aided design (CAD) model of *Ascento*. Further, a static friction coefficient μ_h of 0.8 has been assumed, which is typical for tire on road conditions.

[14]The PD gains for tasks 2), 3) and 5) were tuned each by first adjusting the proportional gain k_p to follow a trajectory with desired aggressiveness. Next, the derivative gain was selected as $k_d = 2\sqrt{k_p}$, which corresponds to ideal damping for a unitary mass harmonic oscillator. In the cases where this choice of k_p lead to oscillations caused by noisy state estimates, we reduced k_p until these would disappear. The cost matrices for state and input cost of the LQR in task 4) were tuned similarly as presented in [2] since the simplified state-space model (36) is a subset of the full model in [2].

that exploits recursive dependencies and maximizes the reuse of quantities that appear multiple times. The QPs arising from the WBC scheme are solved using the state of the art QP-solver *OSQP* [29]. For the solution of the DARE for the LQR, the *Control Toolbox* [30] library was employed. The QP and the DARE get automatically warm-started with the solution of the previous time step. We run the controller at a frequency of $400\,\mathrm{Hz}$ on the onboard computer.[15] The average control period is $1.56\,\mathrm{ms}$, whereof $1.20\,\mathrm{ms}$ are used for the hierarchical optimization of the WBC, $0.11\,\mathrm{ms}$ are used for the evaluation of the model, and the remaining time is attributed to the calculation of the DARE, the state estimator and program overhead. An illustration of the control loop is shown in Fig. 7.

B. Experiments

1) Impact Robustness of Balancing Control: A $2\,\mathrm{kg}$ weight attached to a cord is dropped from a relative height of $1\,\mathrm{m}$ to create a horizontal impact with the robot, as shown in Fig. 8. The response is qualitatively compared to the previous, LQR-based controller[16] running on *Ascento* [2], which fails to stabilize the system, while the controller proposed in this work recovers from the disturbance with a T90 time of ca. $1\,\mathrm{s}$.

2) Adaption to Varying Ground Heights: The experiment shown in Fig. 9 demonstrates how compliance to uneven terrain arises naturally by the proposed WBC scheme and task selection. Namely, by requiring zero roll angle, i.e. $\psi = 0$, the robot remains upright by adapting the leg extensions to account for varying ground heights. This is shown while the robot is balancing and holding its position; but also while driving the exact same mechanism is active. As can be seen, the left leg extension φ_1 stays nearly constant at $1.8\,\mathrm{rad}$, while the right leg extension φ_2 closely follows the disturbance.

3) ZMP-Regulated Curve Driving: To assess how computation of the roll angle reference influences curve driving, we performed two experiments. In the first one, $^{ref}\psi$ was set to $0\,\mathrm{rad}$ and, in the second one, it was dynamically computed to regulate the ZMP towards the center G of the LoS, as proposed in Section III-B3. As can be seen in Fig. 10, this resulted in significantly steadier curve driving when leaning. We assessed this by using the robot's wheel odometry provided by the kinematics-based state estimator.

V. OUTLOOK

In future work, we would like to extend our approach to model the dynamics of impulsive contact events, e.g. using the method outlined in [31]. This could for instance enable synthesis of jumping motions in a model predictive control (MPC) scheme leveraging the full system dynamics.

Further, we would like to improve our state estimation by incorporating measurements from additional sensors, such as cameras. Using nonlinear estimation techniques such as Unscented Kalman Filtering (UKF) [32] or visual-inertial
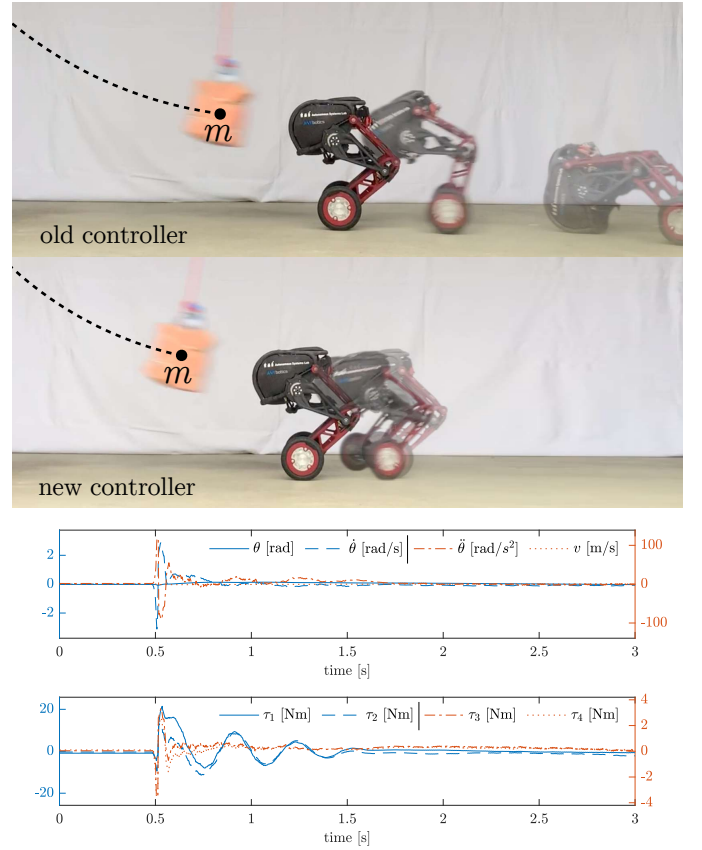
---

[15]I.e. a NUC7I7BNH with $3.5\,\mathrm{GHz}$ dual-core Intel Core i7 processor.

[16]This controller assumed a two-wheeled, inverted pendulum of constant length as model and used a fixed linearization point around the upright equilibrium.

Fig. 8. Impact robustness of balancing control. The images on the top qualitatively show the response to an impact with a $m = 2\,\mathrm{kg}$ load for the previous LQR-based controller [2] and for the WBC scheme proposed in this work. The two graphs below quantitatively show the corresponding response for the proposed WBC scheme. The actuation torques (as introduced in Fig. 2) computed by the WBC are depicted in the bottom graph and the resulting evolution of the ground velocity v and the base pitch angle θ in the upper graph. It is to be noted that the angular acceleration response $\ddot{\theta}$ was calculated based on the current system state $\boldsymbol{q}$, $\boldsymbol{u}$ using (25), (27).
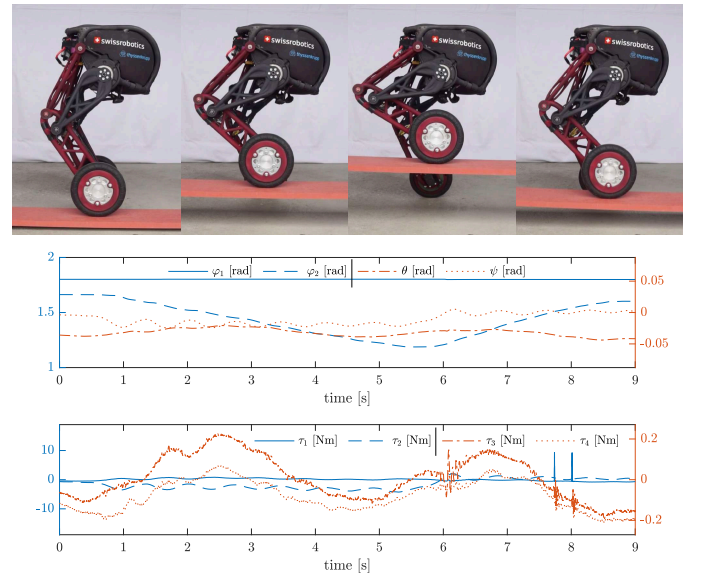

Fig. 9. Adaption to varying ground heights. The robot's right wheel is placed on a plank which is *manually* moved up and down, leading to unpredictable, non-periodic disturbances, as shown in the image sequence. The bottom graph shows the actuation torques computed by the WBC and the top graph the resulting base roll angle, base pitch angle, and hip joint angles (as introduced in Fig. 2). As can be seen, the robot tracks constant base height and zero roll angle by adapting the extension of the right leg accordingly.
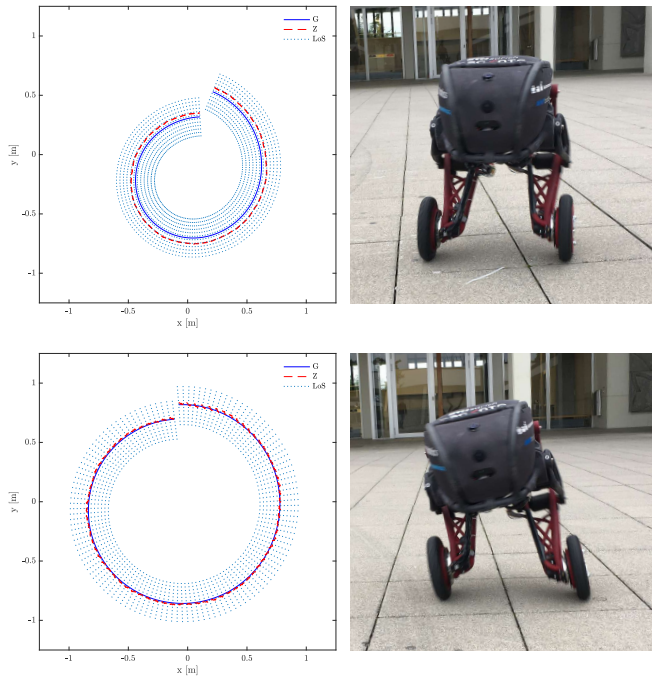
Fig. 10. ZMP-Regulated Curve Driving. The graphs (with snapshots of the robot on the right) show the trajectories that result from driving a curve with constant linear (ground) and angular (yaw) velocity references, where G denotes the center of the LoS and Z the ZMP. The top graph shows the outcome from setting a constant roll angle reference of $0\,\mathrm{rad}$ and the bottom graph the one from dynamically computing the roll angle reference such as to shift the ZMP towards G, which results in the robot leaning "into the curve".

odometry [33] would bring the system one step closer to autonomous deployment.

Finally, the accuracy of the dynamics model could be improved by performing dedicated system identification experiments.

ACKNOWLEDGMENT

REFERENCES

[1] Boston Dynamics. Handle robot reimagined for logistics. Youtube. [Online]. Available: https://youtu.be/5iV_hB08Uns

[2] V. Klemm, A. Morra, C. Salzmann, F. Tschopp, K. Bodie, L. Gulich, N. Küng, D. Mannhart, C. Pfister, M. Vierneisel, *et al.*, "Ascento: A two-wheeled jumping robot," *Proc. IEEE Int. Conf. Robot. Autom.*, pp. 7515–7521, May 2019.

[3] M. Hutter, H. Sommer, C. Gehring, M. Hoepflinger, M. Bloesch, and R. Siegwart, "Quadrupedal locomotion using hierarchical operational space control," *Int. J. Robot. Res.*, vol. 33, no. 8, pp. 1047–1062, 2014.

[4] A. Herzog, L. Righetti, F. Grimminger, P. Pastor, and S. Schaal, "Balancing experiments on a torque-controlled humanoid with hierarchical inverse dynamics," in *Proc. IEEE/RSJ Int. Conf. Intell. Robots Syst.* IEEE, 2014, pp. 981–988.

[5] A. Escande, N. Mansard, and P.-B. Wieber, "Hierarchical quadratic programming: Fast online humanoid-robot motion generation," *Int. J. Robot. Res.*, vol. 33, no. 7, pp. 1006–1028, 2014.

[6] C. D. Bellicoso, C. Gehring, J. Hwangbo, P. Fankhauser, and M. Hutter, "Perception-less terrain adaptation through whole body control and hierarchical optimization," in *Proc. IEEE-RAS 16th Int. Conf. Humanoid Robots*, Nov 2016, pp. 558–564.

[7] D. Kim, J. Lee, J. Ahn, O. Campbell, H. Hwang, and L. Sentis, "Computationally-robust and efficient prioritized whole-body controller with contact constraints," in *Proc. IEEE/RSJ Int. Conf. Intell. Robots Syst.* IEEE, 2018, pp. 1–8.

[8] L. Sentis and O. Khatib, "A whole-body control framework for humanoids operating in human environments," in *Proc. IEEE Int. Conf. Robot. Autom.* IEEE, 2006, pp. 2641–2648.

[9] C. D. Bellicoso, F. Jenelten, P. Fankhauser, C. Gehring, J. Hwangbo, and M. Hutter, "Dynamic locomotion and whole-body control for quadrupedal robots," in *Proc. IEEE/RSJ Int. Conf. Intell. Robots Syst.*, Sept 2017, pp. 3359–3365.

[10] A. W. Winkler, C. Mastalli, I. Havoutis, M. Focchi, D. G. Caldwell, and C. Semini, "Planning and execution of dynamic whole-body locomotion for a hydraulic quadruped on challenging terrain," in *Proc. IEEE Int. Conf. Robot. Autom.* IEEE, 2015, pp. 5148–5154.

[11] M. Bjelonic, C. D. Bellicoso, Y. de Viragh, D. Sako, F. D. Tresoldi, F. Jenelten, and M. Hutter, "Keep rollin–whole-body motion control and planning for wheeled quadrupedal robots," *IEEE Robot. Autom. Lett.*, vol. 4, no. 2, pp. 2116–2123, April 2019.

[12] Y. de Viragh, M. Bjelonic, C. D. Bellicoso, F. Jenelten, and M. Hutter, "Trajectory optimization for wheeled-legged quadrupedal robots using linearized zmp constraints," *IEEE Robot. Autom. Lett.*, vol. 4, no. 2, pp. 1633–1640, April 2019.

[13] Boston Dynamics. Introducing Handle. Youtube. [Online]. Available: https://youtu.be/-7xvqQeoA8c

[14] B. Siciliano, L. Sciavicco, L. Villani, and G. Oriolo, *Robotics: Modelling, Planning and Control*, ser. Advanced Textbooks in Control and Signal Processing. Springer London, 2010.

[15] M. Kamel, K. Alexis, and R. Siegwart, "Design and modeling of dexterous aerial manipulator," in *Proc. IEEE/RSJ Int. Conf. Intell. Robots Syst.*, Oct 2016, pp. 4870–4876.

[16] R. S. Hartenberg and J. Danavit, *Kinematic Synthesis of Linkages*. New York, San Francisco, Toronto, London: McGraw-Hill Book Company, 1964.

[17] W. Khalil, "Dynamic modeling of robots using recursive newton-euler techniques." vol. 1, 06 2010, pp. 19–31.

[18] Briot and Khalil, *Dynamic Modeling of Parallel Robots*, ser. Dynamics of Parallel Robots. Mechanisms and Machine Science. Springer Cham, 2015, vol. 35.

[19] W. Khalil and E. Dombre, *Modeling, Identification and Control of Robots*, ser. Kogan Page Science paper edition Modeling, identification & control of robots. Elsevier Science, 2004.

[20] B. Siciliano and O. Khatib, *Springer Handbook of Robotics*. Springer, 2016.

[21] M. Iwamura and M. Nagao, "A method for computing the hessian tensor of loop closing conditions in multibody systems," *Multibody System Dynamics*, vol. 30, no. 2, pp. 173–184, 2013.

[22] M. Vukobratović and B. Borovac, "Zero-moment point – thirty five years of its life," *Int. J. Humanoid Robot.*, vol. 1, no. 01, pp. 157–173, 2004.

[23] C. Glocker, "Dynamik von Starrkörpersystemen mit Reibung und Stößen," Ph.D. dissertation, Technische Universität München, 1995.

[24] H. Essén, "Average angular velocity," *European Journal of Physics*, vol. 14, no. 5, p. 201, 1993.

[25] Open Source Robotics Foundation, "Gazebo." [Online]. Available: http://gazebosim.org

[26] S. Russell, "ODE – open dynamics engine." [Online]. Available: http://www.ode.org

[27] M. Bloesch, M. Hutter, M. Hoepflinger, S. Leutenegger, C. Gehring, C. David Remy, and R. Siegwart, "State estimation for legged robots - consistent fusion of leg kinematics and IMU," July 2012.

[28] G. Guennebaud, B. Jacob, *et al.*, "Eigen v3." [Online]. Available: http://eigen.tuxfamily.org

[29] B. Stellato, G. Banjac, P. Goulart, A. Bemporad, and S. Boyd, "Osqp: An operator splitting solver for quadratic programs," in *2018 UKACC 12th International Conference on Control (CONTROL)*. IEEE, 2018, pp. 339–339.

[30] M. Giftthaler, M. Neunert, M. Stäuble, and J. Buchli, "The Control Toolbox - an open-source C++ library for robotics, optimal and model predictive control," pp. 123–129, May 2018.

[31] J. Hwangbo, J. Lee, and M. Hutter, "Per-contact iteration method for solving contact dynamics," *IEEE Robot. Autom. Lett.*, vol. 3, no. 2, pp. 895–902, April 2018.

[32] E. A. Wan, R. Van Der Merwe, *et al.*, "The unscented kalman filter," *Kalman filtering and neural networks*, vol. 5, no. 2007, pp. 221–280, 2001.

[33] D. Scaramuzza and F. Fraundorfer, "Visual odometry [tutorial]," *IEEE robotics & automation magazine*, vol. 18, no. 4, pp. 80–92, 2011.